Experimental cross-section measurement of the nuclear reactions induced by protons on ^{159}Tb: Evaluation of the ^{155}Dy/^{155}Tb precursor system

Michele Colucci [a,b,*,1], Filippo Carlo Bolchini [a,b,1], Lorenzo Confalonieri [a,b], Ferid Haddad [c,d], Etienne Nigron [d], Flavia Groppi [a,b], Simone Manenti [a,b]

[a] *Department of Physics, University of Milan, via Celoria, 16, Milan (MI), 20133, Italy*
[b] *LASA, University of Milan and INFN-Milan, via F.lli Cervi, 201, Segrate (MI), 20090, Italy*
[c] *Laboratoire Subatech, CNRS/IN2P3, IMT Atlantique, Nantes Université, 4, rue Alfred Kastler, Nantes, 44307, France*
[d] *GIP Arronax, 1, rue Aronnax, Saint-Herblain, 44817, France*

ARTICLE INFO

ABSTRACT

^{149,152,155,161}Tb have recently been under the lens of research in nuclear medicine due to their physical characteristics, which allow them to be used in various applications in both diagnosis and therapy. Performing the optimization of the production methods of these terbium radioisotopes is of great research interest. In this work, the viability of the production of ^{155}Tb ($T_{1/2}$ = 5.32 d) via the ^{155}Dy/^{155}Tb precursor system was studied and discussed from a theoretical point of view. The production of ^{155}Dy, alongside its contaminants, was accomplished through the ^{159}Tb(p,x) nuclear reactions. The cross-sections of these reactions were studied in the 37.5–62 MeV energy range using the stacked-foils technique. The study of the yield of the indirectly produced ^{155}Tb give promising estimations for an implementation of the ^{155}Dy/^{155}Tb precursor system.

1. Introduction

The field of nuclear medicine is currently developing in the direction of theranostics, a tailor-made radiopharmaceutical therapy that aims to enhance the therapeutic effects of radioactive substances while reducing treatment toxicities (Naskar and Lahiri, 2021; Qaim et al., 2021). The term theranostics in nuclear medicine refers to the pairing of therapeutic-diagnostic radionuclides linked to a compound (called carrier or vector) that targets a particular kind of cancer cells. On the one hand, therapeutic radioisotopes decay by releasing particles like α, β⁻ or Auger electrons, which release energy over a short distance leading to ionization or bond breakage. On the other hand, diagnostic radioisotopes decay by releasing gamma rays or emitting gamma rays after the annihilation of β⁺ particles. Gamma rays are highly penetrating radiations that can be collected outside the body for imaging purposes (Herzog et al., 1993; Rösch et al., 2017).

Tb is a unique element that provides four radionuclides decaying through all types of radiations (^{149}Tb, ^{152}Tb, ^{155}Tb and ^{161}Tb) useful for medical application, that makes it the perfect tool for the theranostic approach, proposed for the first time by the PSI research team (Müller et al., 2012, 2018). The chemistry of an element remains consistent across its isotopes, allowing the same radiopharmaceutical to be labeled with two different terbium radioisotopes. This

enables precise assessment of the dose delivered before treatment, as the radiopharmaceutical's behavior remains consistent in both the diagnostic and therapeutic phases, facilitating a personalized approach to therapy (Qaim, 2019).

^{149}Tb is a short-lived ($T_{1/2}$ = 4.12 h National Nuclear Data Center (2024)) radionuclide and it is the only α-emitter of the Tb family. It is a candidate for targeted alpha therapy (TAT). Moreover, ^{149}Tb is also a β⁺ emitter, allowing its detection through Positron Emission Tomography (PET) exams simultaneously with ^{149}Tb radiopharmaceutical administration. The main drawbacks of ^{149}Tb are the feasibility of its large-scale production (production is at the moment restricted to few sites able to perform the ISOL technique using mass separation). The impact of its complicated decay scheme on the radio-toxicity of this radionuclide needs to be inferred precisely, in particular due to its various long-lived daughter nuclei such as ^{149}Gd ($T_{1/2}$ = 9.28 d), ^{145}Eu ($T_{1/2}$ = 5.93 d), ^{145}Sm ($T_{1/2}$ = 340 d), ^{149}Eu ($T_{1/2}$ = 93.1 d) and ^{145}Pm ($T_{1/2}$ = 17.7 y) (Naskar and Lahiri, 2021; National Nuclear Data Center, 2024; Müller et al., 2017).

^{152}Tb ($T_{1/2}$ = 17.5 h National Nuclear Data Center (2024)) is a β⁺ emitter that can be used as a diagnostic tool and for dosimetry and the monitoring of the distribution of the ^{149,161}Tb isotopes which act as the

---

therapeutic counterparts (Naskar and Lahiri, 2021; National Nuclear Data Center, 2024; Nedrow and Anderson, 2011).

^{155}Tb ($T_{1/2}$ = 5.32 d National Nuclear Data Center, 2024) is a potential Single Photon Emission Computed Tomography (SPECT) candidate thanks to its gamma emissions at 86.55 keV (32%) and 105.32 keV (25.1%) (National Nuclear Data Center, 2024). Furthermore, it can be used for dosimetry calculation before therapy, for example in a matched pair with ^{161}Tb or ^{149}Tb (Naskar and Lahiri, 2021; Müller et al., 2019).

^{161}Tb ($T_{1/2}$ = 6.89 d National Nuclear Data Center, 2024) mainly decays by emitting β^- particles, but it also has the characteristic of emitting Auger and conversion electrons. On average, 2.24 Auger and conversion electrons are emitted per β^- particle (National Nuclear Data Center, 2024). This characteristic of ^{161}Tb could make it an alternative to ^{177}Lu for cancer treatment as it can have a higher killing potential if internalized within the cell (Müller et al., 2019; Lehenberger et al., 2011).

The production of Tb radioisotopes is still a challenge due to the non-monoisotopic Gd target material, their production cross-sections, and the complexity of radiochemical separations of lanthanides (Naskar and Lahiri, 2021; Pupillo et al., 2023; Qaim et al., 2018). In order to facilitate the diffusion of Tb radioisotopes in clinical practices, the main challenge to overcome is obtaining high amount of said radionuclides (in the order of GBq) while maintaining a high radionuclidic purity.

Regarding the production of ^{155}Tb, different methods have been studied. The direct production using medical cyclotron accelerated protons on enriched ^{155}Gd and ^{156}Gd targets permit to reach acceptable yield but with a limited purity (lower than 93% and 89% respectively) of the product mainly due to the current enrichment of the Gd target and to the unavoidable co-production of ^{156g}Tb that is not separable from the radionuclide of interest without off-line mass separation, that, in any case, will lead to a reduction of the yield (Dellepiane et al., 2022). The ^{155}Gd(d,2n)^{155}Tb nuclear reaction allows to obtain a 3 times higher yield but with a lower purity (<90%) due to the presence of ^{154,156}Tb (Wang et al., 2023). Very low yield and purity are reached with other direct reactions induced by light ions, such as ^{nat}Dy(d,x)^{155}Tb (Colucci et al., 2022), or ^{nat}Gd(α,x)^{155}Tb (Moiseeva et al., 2022) nuclear reactions. However, an indirect production method exploiting medium-energy light ions is possible, through the production of ^{155}Dy and its subsequent decay in ^{155}Tb (Moiseeva et al., 2022, 2023). With this technique very high radionuclidic purity is achievable.

In this work, the excitation function of the ^{159}Tb(p,5n)^{155}Dy nuclear reaction was studied, alongside the excitation functions of the main Dy contaminants (i.e. ^{157,159}Dy) and of other radionuclides produced in the reaction. The cross-section results are compared with previous experimental data by Steyn et al. (2014), Tárkányi et al. (2017) and Engle et al. (2016). This new set of data enriches the nuclear libraries and is used in this paper to discuss the Thick Target Yields (TTY) of production of ^{155}Tb obtained via ^{155}Dy/^{155}Tb precursor system in order to evaluate the potential of this route.

2. Material and methods

The excitation functions were measured by irradiating 16 different thin ^{159}Tb metallic targets with protons, using the stacked-foils technique. Four different stacks, each containing 4 terbium foils, were used to cover the proton energy range from 37.5 to 62 MeV. In every stack, each Tb foil was followed by a 16 μm Al catcher foil, which served also as monitor foil as long as it was not adjacent to another Al foil. Thick Al foils (250 μm) were used as energy degraders, while some Ti foils were positioned in the stack as monitor foils. In the stack, some Dy foils were present for a parallel experiment, not related to this work. The uniformity of each foil was verified using an analogical thickness gauge (sensibility equal to 0.1 μm). The mass and surface area of each foil were measured with a high precision weighting scale and a caliber (of uncertainties equal to 10^{-5} g and 10^{-5} m respectively), so to determine the mass thickness of each foil. The uncertainty on the

Table 1

Characteristics of the metallic foils used in this work. The mass thickness range shows the minimum and maximum measured values for the mass thickness of that specific type of foil. The relative uncertainty associated with the mass thickness of all foils was set equal to 2%.

Material	Nominal thickness	Size	Nominal purity	Mass thickness (mg cm^{-2})
^{159}Tb	25 μm ± 0.25%	5 × 5 cm^2	99%	20.84–25.51
^{27}Al (catcher)	16 μm ± 0.25%	Roll	99%	4.46
^{27}Al (degrader)	250 μm	10 × 10 cm^2	99%	67.86–68.54 6
^{nat}Ti	20 μm	10 × 10 cm^2	99.6%	8.06–8.226

Table 2

Mean energy values of the proton beam in each Tb foil.

Stack	E_1 (MeV)	E_2 (MeV)	E_3 (MeV)	E_4 (MeV)
1st	61.8 ± 0.4	59.8 ± 0.4	57.7 ± 0.4	55.0 ± 0.6
2nd	56.0 ± 0.4	54.2 ± 0.4	52.3 ± 0.5	50.2 ± 0.6
3rd	50.7 ± 0.4	48.7 ± 0.4	46.6 ± 0.5	43.6 ± 0.7
4th	44.6 ± 0.4	42.5 ± 0.5	40.3 ± 0.6	37.5 ± 0.7

mass thickness is set to 2% in order to account for the non-uniformity of the foil thickness. The foils characteristics are summarized in Table 1. Successively, the foils were cut in squares of area 2.5 × 2.5 cm^2 to be placed in the stack holder for the irradiation.

All the metallic foils have been purchased from GoodFellow Corporation (Huntingdon, UK).

2.1. Irradiation setup

The irradiation was carried out by accelerating protons with the high-intensity cyclotron (IBA-C70XP, K = 70) of GIP ARRONAX research center (Saint-Herblain, France) (Haddad et al., 2008). Each stack was positioned in air at a distance of about 8 cm from the end of the beamline, which is closed by a 50 μm Kapton layer. The shape of the beam was checked by irradiating a Al$_2$O$_3$ scintillating foil, to ensure a well-collimated and centered beam on the stack. The four stacks were irradiated in two distinct irradiation sessions at a constant beam current of 150 nA for 1 h each. The mean beam energies directed within each foil (detailed in Table 2) were deliberately chosen to guarantee an overlap in the energy ranges during the irradiation of successive stacks. This selection facilitates the identification of potential bias between each experiment, as it accentuates any discontinuity in the curve formed by the data points. The current stability during each irradiation was monitored using a beam dump equipped with a charge integrator. The total charge of the incident beam was then determined by the ratio between the measured cross-sections of the ^{nat}Ti(p,x)^{48}V, ^{nat}Ti(p,x)^{46}Sc, and ^{27}Al(p,x)^{24}Na monitor reactions, calculated using a fictitious charge Q* = 1 C, and the IAEA recommended values (Hermanne et al., 2018).

2.2. Measurements

The activity measurements of the produced radionuclides were carried out at the LASA Laboratory (Segrate, Italy) using HPGe detectors. Each detector was calibrated with certified ^{133}Ba and ^{152}Eu calibration sources (CercaLEA, France). In particular, the ^{133}Ba source was necessary in order to determine the efficiency curve at low energies by exploiting its 53.16 keV (I_γ = 2.14 *3* %), 80.99 keV (I_γ = 32.9 *3*%), and 160.61 keV (I_γ = 0.638 *5*%) gamma emissions. This was crucial for measuring ^{159}Dy, whose only measurable gamma emission is at 58 keV (I_γ = 2.27 *13*%). The irradiated targets were positioned on top of a spacer, with the beam entrance side facing the detector crystal in the same geometry as the calibration. The measurements were carried out in the time interval between 2 days and 4 months after each irradiation. The duration of the measurements was between 20 min and 2 days for short- and medium-lived radionuclides, and from 2 to 7 days for the long-lived radionuclides such as ^{159}Dy and ^{151,153}Gd. The radionuclides

Table 3

List of detected radionuclides: symbol, decay mode, half-life, gamma emission used to determine the activities alongside their characteristics (National Nuclear Data Center, 2024), and production reactions involved. Peaks labeled "b" combine similar-energy gamma emissions treated as a single peak. Uncertainties on $T_{1/2}$, E_γ, and I_γ values are italicized and pertain to the last significant figures.

Nuclide	$T_{1/2}$	E_γ (keV)	I_γ (%)	Contributing reactions	E_{th} (MeV)
^{155}Dy	9.9 2 h	184.564 4	3.39 8	^{159}Tb(p,5n)	33.656
ϵ, β^+: 100%		226.918^a 4	68.7 16		
		271.056 9	1.22 7		
		664.173 18	2.25 6		
		905.515 21	2.46 7		
^{157}Dy	8.14 4 h	326.336 10	93 3	^{159}Tb(p,3n)	17.141
ϵ, β^+: 100%					
^{159}Dy	144.4 2 d	58.0 1	2.27 13	^{159}Tb(p,n)	1.1549
ϵ: 100%					
^{153}Tb	2.34 1 d	212.00 2	28.5 19	^{159}Tb(p,t4n)	38.407
ϵ, β^+: 100%				^{153}Dy decay	
^{154g}Tb	21.5 h 4 h	123.07^a 3	26 4	^{159}Tb(p,t3n)	31.45
ϵ, β^+: 100%		873.21^a 4	5.3 5	^{159}Tb(p,d4n)	37.75
		1274.436^a 6	10.5 8	^{159}Tb(p,p5n)	39.98
		1291.31 13	6.9 5		
^{154m1}Tb	9.4 4 h	123.07^a 3	31 6	^{159}Tb(p,t3n)	31.45
ϵ, β^+: 78.2 7%		540.18 6	20 3	^{159}Tb(p,d4n)	37.75
IT: 18.8 7%		649.44^a 6	11.2 18	^{159}Tb(p,p5n)	39.98
		873.21^a 4	9.4 16		
^{154m2}Tb	22.7 5 h	123.07^a 3	43 8	^{159}Tb(p,t3n)	31.45
ϵ, β^+: 98.2 6%		141.33 3	7.3 9	^{159}Tb(p,d4n)	37.75
IT: 1.8 6%		247.94 3	79 10	^{159}Tb(p,p5n)	39.98
		346.70 4	69 7		
		426.78 7	17.3 12		
		649.44^a 6	8.6 9		
		873.21^a 4	3.4 4		
^{155}Tb	5.32 6 d	86.55 3	32.0 18	^{159}Tb(p,t2n)	22.226
ϵ: 100%		105.318 3	25.1 13	^{159}Tb(p,d3n)	28.523
		148.64 1	2.65 14	^{159}Tb(p,p4n)	30.761
		161.29 1	2.76 15	^{155}Dy decay	
		163.28 1	4.44 23		
		268.56 1	0.71 6		
		340.67 1	1.18 7		
		367.3723^b 9	2.31 23		
^{156}Tb	5.35 10 d	88.97 2	18 3	^{159}Tb(p,tn)	15.27
ϵ, β^+: 100%		199.19 4	41 5	^{159}Tb(p,d2n)	21.567
		296.49 4	4.5 4		
		356.38 5	13.6 13		
		422.34 6	8.0 8		
		534.29 6	67 6		
		1154.07 15	10.4 10		
		1159.03 15	7.2 7		
		1222.44 9	31 3		
		1421.67 9	12.2 12		
^{151}Gd	123.9 10 d	153.60 1	6.4 2	^{159}Tb(p,α5n)	31.032
ϵ: 100%		174.70 1	2.96 20	^{151}Tb decay	
		243.29 3	5.6 4		
^{153}Gd	240.4 10 d	97.43100 21	30.0 3	^{159}Tb(p,α3n)	16.1011
ϵ: 100%		103.18012 17	22.1 3	^{159}Tb(p,2tn)	27.5051
				^{153}Tb decay	

^{a} Denotes emissions with superposition.

whose cross-section was measured are listed in Table 3, along with their half-lives and nuclear data regarding their decay properties and production reactions.

3. Results

The experimental cross-section values of the radionuclides listed in Tables 4 and 5 were evaluated by measuring the activity produced on the Tb targets. The cross-section values $\sigma(E)$ (mb) were computed using the following equation:

$$\sigma(E) = \frac{C}{LT \cdot \varepsilon \cdot I_\gamma} \cdot \frac{M \cdot \mathbf{e}}{\lambda \cdot Q \cdot N_A \cdot \rho x} \cdot D(RT) \cdot G(t_{irr}) \cdot e^{\lambda t_{dec}} \cdot 10^{-27} \quad (1)$$

where E (MeV) is the mean energy of the proton beam in the target foil, C are the net counts of the photo-peak of energy E_γ, ε is the detector efficiency at energy E_γ, I_γ is the abundance of the gamma emission of energy E_γ, LT (s) is the Live Time of the measurement, RT (s) is the Real Time of the measurement (given by the sum of

LT and the dead time of the measurement), M is the atomic mass (in g mol^{-1}) of the target material, $\mathbf{e}$ is the proton charge (C), λ is the decay constant (s^{-1}) of the detected radionuclide, Q is the total charge of the incident proton beam (C), N_A is the Avogadro number (mol^{-1}), ρx is the mass thickness of the target foil (g cm^{-2}), t_{irr} (s) is the duration of irradiation, t_{dec} (s) is the time interval between the End Of Bombardment (EOB) and the beginning of measurements. Two correction factors are also present: the *growing factor* $G(t_{irr})$ which takes into account the produced radionuclide decay during irradiation, and the *decay factor* $D(RT)$ which takes into account the decay of the radionuclides during the measurements.

$$G(t_{irr}) = \frac{\lambda \cdot t_{irr}}{1 - e^{-\lambda \cdot t_{irr}}} \quad (2)$$

$$D(RT) = \frac{\lambda \cdot RT}{1 - e^{-\lambda \cdot RT}} \quad (3)$$

Table 4

Values of the cross-sections σ, with their respective uncertainties, of the detected Dy and Gd isotopes. The average beam energy E and energy uncertainty δE in each target are also presented. The apex "c" indicates the cumulative cross-sections, while the apex "i" indicates the direct cross-sections. The cumulative ^{153}Gd cross-section is due to the ^{153}Tb decay into ^{153}Gd, while the cumulative ^{151}Gd cross-section is due to the ^{151}Tb decay into ^{151}Gd.

$E \pm \delta E$ (MeV)	^{155}Dy (mb)	^{157}Dy (mb)	^{159}Dy (mb)	^{151}Gd^c (mb)	^{153}Gd^c (mb)	^{153}Gd^i (mb)
37.5 ± 0.7	2.7 ± 0.2	292 ± 16	25 ± 3		3.05 ± 0.13	3.05 ± 0.13
40.3 ± 0.6	62 ± 3	207 ± 11	20 ± 2		9.8 ± 0.4	9.8 ± 0.4
42.5 ± 0.5	190 ± 8	158 ± 9	15 ± 2		15.1 ± 0.6	15.1 ± 0.6
43.6 ± 0.7	238 ± 11	147 ± 8	14 ± 2		16.8 ± 0.7	16.8 ± 0.7
44.6 ± 0.4	322 ± 14	135 ± 7	14 ± 2		16.8 ± 1.1	16.8 ± 1.1
46.6 ± 0.5	434 ± 20	126 ± 7	13 ± 2		18.7 ± 1.2	18.7 ± 1.2
48.7 ± 0.4	534 ± 23	115 ± 6	12 ± 2		17.8 ± 1.1	17.8 ± 1.1
50.2 ± 0.6	595 ± 26	118 ± 6	11.3 ± 1.2	0.22 ± 0.07	18.8 ± 1.0	18.8 ± 1.0
50.7 ± 0.4	558 ± 24	107 ± 6	12.5 ± 1.5	1.0 ± 0.3	17.1 ± 1.1	17.1 ± 1.1
52.3 ± 0.5	561 ± 27	103 ± 6	10.4 ± 0.9	0.49 ± 0.09	16.8 ± 0.7	16.8 ± 0.7
54.2 ± 0.4	515 ± 24	100 ± 6	11.5 ± 1.4	1.04 ± 0.11	15.7 ± 0.6	15.7 ± 0.6
55.0 ± 0.6	505 ± 24	95 ± 5	9.7 ± 1.0	0.84 ± 0.15	14.3 ± 0.8	14.3 ± 0.8
56.0 ± 0.4	436 ± 21	94 ± 5	10.5 ± 1.4	2.80 ± 0.19	14.9 ± 0.6	13.5 ± 0.6
57.7 ± 0.5	427 ± 27	91 ± 5	9.1 ± 0.9	2.1 ± 0.2	14.7 ± 0.6	14.0 ± 0.6
59.8 ± 0.4	314 ± 15	82 ± 5	8.5 ± 0.9	4.0 ± 0.3	13.6 ± 0.6	10.9 ± 0.6
61.8 ± 0.4	276 ± 17	83 ± 5	8.8 ± 1.1	7.6 ± 0.4	17.2 ± 0.8	7.9 ± 0.9

Table 5

Values of the cross-sections σ, with their respective uncertainties, of the detected Tb isotopes. The average beam energy E and energy uncertainty δE in each target are also presented. The apex "c" indicates the cumulative cross-sections, while the apex "i" indicates the direct cross-sections. The cumulative ^{153}Tb cross-section is due to the ^{153}Dy decay into ^{153}Tb, while the ^{155}Tb cross-section is due to the ^{155}Dy decay into ^{155}Tb and the ^{156}Tb cross-section is due to the ^{156m1,m2}Tb decay into ^{156}Tb.

$E \pm \delta E$ (MeV)	^{153}Tb^c (mb)	^{154m1}Tb (mb)	^{154m2}Tb (mb)	^{155}Tb^c (mb)	^{155}Tb^i (mb)	^{156}Tb^c (mb)
37.5 ± 0.4				5.6 ± 0.2	2.62 ± 0.13	25.1 ± 1.0
40.3 ± 0.4				75 ± 3	6 ± 2	50 ± 2
42.5 ± 0.3				225 ± 9	16 ± 8	76 ± 3
43.6 ± 0.4			0.16 ± 0.03	277 ± 11	18 ± 11	81 ± 3
44.6 ± 0.3			0.41 ± 0.09	386 ± 15	34 ± 15	94 ± 4
46.6 ± 0.4		5.8 ± 1.3	0.26 ± 0.04	550 ± 21	45 ± 19	111 ± 5
48.7 ± 0.4		8 ± 2	0.36 ± 0.04	626 ± 25	38 ± 19	115 ± 5
50.2 ± 0.4		6.8 ± 1.5	0.40 ± 0.04	734 ± 29	79 ± 17	127 ± 5
50.7 ± 0.4		10 ± 2	0.51 ± 0.04	672 ± 28	62 ± 19	123 ± 5
52.3 ± 0.4		7.2 ± 2.0	0.59 ± 0.07	708 ± 28	97 ± 29	112 ± 5
54.2 ± 0.4		15 ± 3	0.72 ± 0.03	690 ± 27	130 ± 26	132 ± 6
55.0 ± 0.5		7.8 ± 1.6	0.58 ± 0.07	655 ± 25	102 ± 26	124 ± 6
56.0 ± 0.4	1.40 ± 0.14	20 ± 3	1.47 ± 0.13	622 ± 24	148 ± 23	133 ± 6
57.7 ± 0.5	0.73 ± 0.09	21 ± 4	0.84 ± 0.08	626 ± 24	159 ± 24	125 ± 6
59.8 ± 0.5	2.72 ± 0.17	27 ± 4	1.95 ± 0.15	518 ± 20	174 ± 16	110 ± 5
61.8 ± 0.4	9.3 ± 0.5	43 ± 6	3.0 ± 0.2	476 ± 19	173 ± 15	112 ± 5

The uncertainty on the photo-peak net counts C has been kept lower than 10% by increasing the LT according to the intensity of the source.

The experimental excitation functions are presented in Figs. 1 to 13 and compared with previous experimental measurements (Steyn et al., 2014; Tárkányi et al., 2017; Engle et al., 2016), and with the TALYS 1.96 (Koning and Rochman, 2012; Koning et al., 2019) computer simulations ran with default settings.

3.1. ^{155}Dy

The ^{155}Dy excitation function is shown in Fig. 1. It can be seen that other works data tend to underestimate this work measurement at energies higher than 50 MeV, but all datasets follow the same overall trend. The TALYS 1.96 simulation seems to be shifted to lower energies, not accurately reproducing the experimental results. The measurements used for estimating the ^{155}Dy were carried out in the first 4–5 days after the end of irradiation due to the relatively short half-life of this radionuclide ($T_{1/2}$ = 9.9 h).

As shown in Table 3 the most abundant gamma emission for this radionuclide is the 226.918 keV emission. Unfortunately, this emission
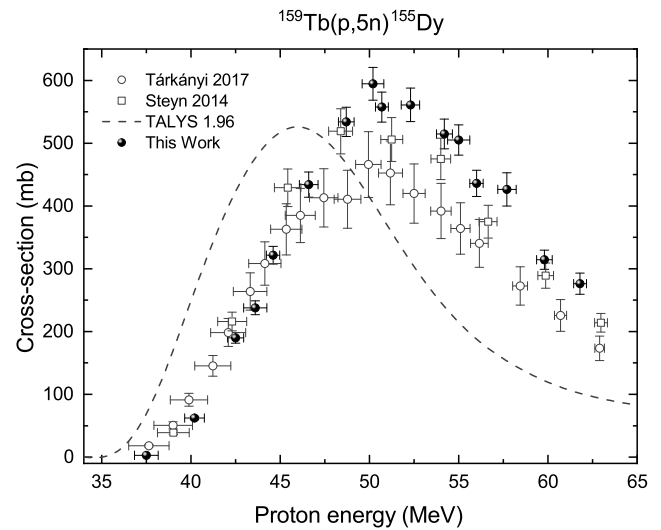

Fig. 1. Comparison between this work ^{155}Dy excitation function and other studies results (Tárkányi et al., 2017; Steyn et al., 2014) and the TALYS 1.96 simulation.

overlaps with the 226.95 keV gamma emission of ^{155}Tb ($T_{1/2}$ = 5.32 days). Moreover, being ^{155}Dy the parent of ^{155}Tb the activities of the two radionuclides are linked. Nevertheless, by solving the Bateman equations for this couple of radionuclides a simple biexponential function is obtained:

$$\left(\frac{C}{LT \cdot \varepsilon}\right)_{photo-peak}(t_{dec}) = a_1 e^{-\lambda_1 t_{dec}} + a_2 e^{-\lambda_2 t_{dec}} \quad (4)$$

In this case $a_{1,2}$ do not represent directly the activities of the two radionuclides, but they are the fitting parameters, from which the ^{155}Dy and ^{155}Tb activities at the EOB can be derived:

$$a_1 = A_1^{EOB} \cdot \left(I_{\gamma 1} + I_{\gamma 2} \frac{\lambda_1}{\lambda_2 - \lambda_1}\right) \quad (5)$$

$$a_2 = I_{\gamma 2} \cdot \left(\lambda_2 N_2^{EOB} - A_1^{EOB} \frac{\lambda_2}{\lambda_2 - \lambda_1}\right) \quad (6)$$

In Eqs. (5) and (6), A_1^{EOB} and $I_{\gamma 1}$ are the EOB activity and abundance of the 226.918 keV gamma emission of ^{155}Dy, while A_2^{EOB} and $I_{\gamma 2}$ are the respective terms of the peak at 226.95 keV of ^{155}Tb.

Thus, to separate the two contributions in the ~226 keV peak a bi-exponential fit method was applied: this procedure is illustrated in Fig. 2. It can be noted that the half-lives are in accordance with the data present in the literature (see Table 3).

3.2. ^{157}Dy

Fig. 3 presents the ^{157}Dy excitation function. This work data aligns well with previous studies. The TALYS 1.96 simulation tends to underestimate the experimental excitation functions considered in this work.

3.3. ^{159}Dy

From Fig. 4, it can be seen that this work ^{159}Dy excitation function aligns well with data from previous studies (Steyn et al., 2014; Tárkányi et al., 2017). At higher energy, the points of Engle et al. (2016) seems to underestimate the cross-section in the whole range, while the TALYS 1.96 simulation tends to overestimate the experimental excitation functions considered in this work. The measurements used for estimating the ^{159}Dy excitation function were acquired not before 5 weeks after the end of irradiation. This is because, as shown in Table 3, ^{159}Dy has a single low abundance (2.27%) gamma emission at 58.0 keV, that is a critical region for p-type HPGe detectors since
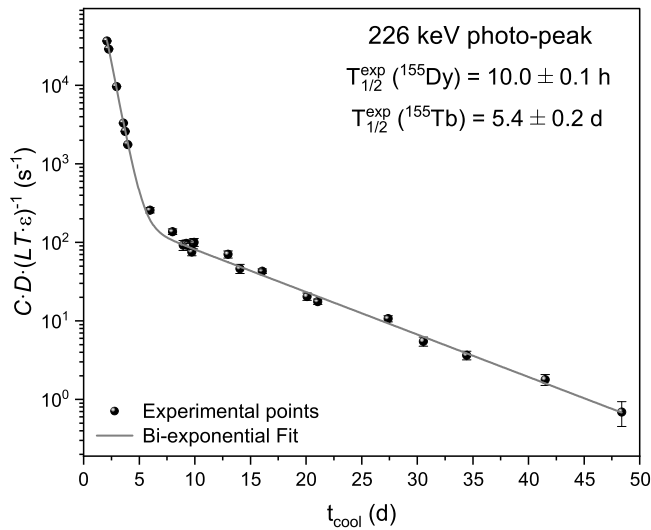
Fig. 2. Experimental $\frac{C}{LT\cdot\varepsilon}$ values for the 226 keV photopeak. The $\frac{C}{LT\cdot\varepsilon}$ were measured multiple times at different cooling times after EOB in order to separate the EOB contributions of ^{155}Dy and ^{155}Tb in the resulting photopeak. The fit was carried out using Eq. (4). The experimental decay times are reported.
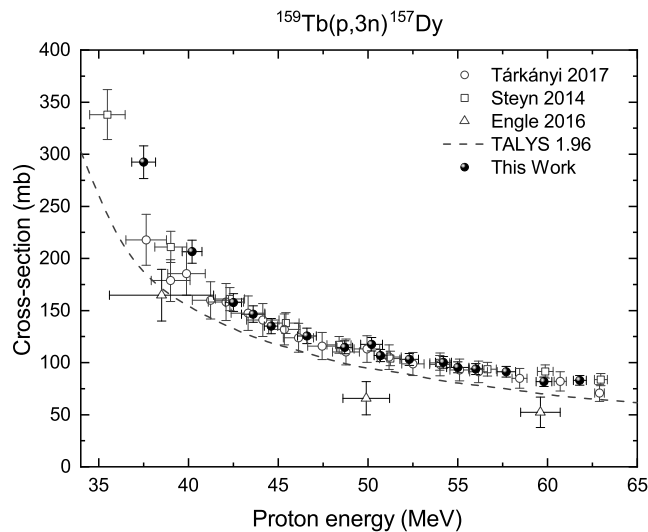

Fig. 3. Comparison between this work ^{157}Dy excitation function and other studies results (Tárkányi et al., 2017; Steyn et al., 2014; Engle et al., 2016) and the TALYS 1.96 simulation.

the efficiency varies rapidly. This, combined with the fact that the ^{159}Dy cross-section is considerably lower compared to the other produced radionuclides, makes the accurate estimation of this radionuclide cross-section difficult in the first days after the end of irradiation. Furthermore, the half-life of ^{159}Dy is 144.4 days meaning that to obtain a satisfactory low uncertainty on the counts C in Eq. (1) long measurements were required. The calibration with ^{133}Ba permitted us to accurately determine the efficiency of detection.

Another aspect that must be taken into consideration is that the only gamma emission of ^{159}Dy overlaps with the ^{155}Tb 57.983 keV gamma emission. The latter gamma emission is not very abundant ($I_\gamma\% = 0.205\%$) but, since the amount of produced ^{155}Tb is much higher compared with ^{159}Dy, we waited 35 days to reduce the activity of ^{155}Tb at least by a factor one hundred. After this time, ^{155}Tb counts were subtracted manually from the 58.0 keV gamma emission of ^{159}Dy, since a good estimate of the ^{155}Tb activity was still possible using other gamma lines.
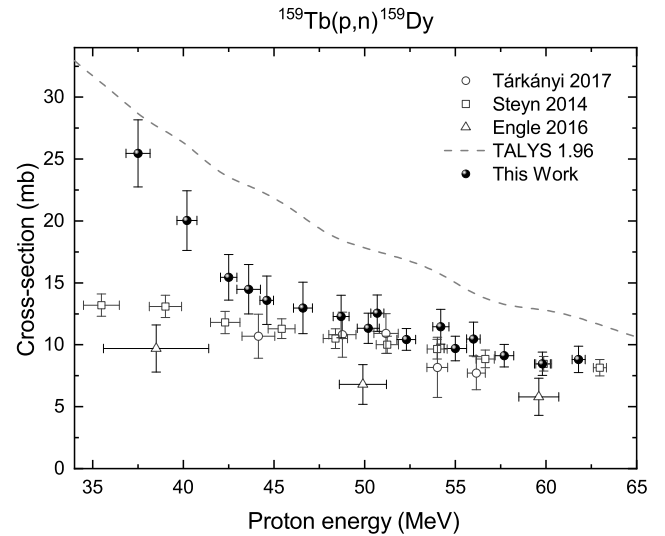

Fig. 4. Comparison between this work ^{159}Dy excitation function and other studies results (Tárkányi et al., 2017; Steyn et al., 2014; Engle et al., 2016) and the TALYS 1.96 simulation.

3.4. $^{153}Tb^c$

Fig. 5 represents the ^{153}Tb cumulative excitation function. Indeed, it was not possible to separate the contribution of direct production and the ^{153}Tb obtained from the decay of the co-produced ^{153}Dy ($T_{1/2} = 6.4$ h) because, by the time we started the measurements, the latter was no longer measurable. It can be seen that data from other works are considerably higher than the data from this work for energies greater than 56 MeV. This could be caused by a possible overlapping between the analyzed ^{153}Tb gamma emissions and other nuclei emissions. For example, the 101.2 keV, 102.4 keV and 103.3 keV emissions of ^{155}Tb could have influenced the measure of the 102.3 keV ^{153}Tb emission. The same concept applies to the 109.8 keV ^{153}Tb emission and the 111.9 keV ^{156g}Tb emission. In this work, only the 212.0 keV ^{153}Tb emission was used. However these considerations do not apply to the work of Steyn et al. (2014), since in that case only the emission at 212.0 keV was used, even if with a slightly different intensity, $I_\gamma = 31.0\%$, that in any case is not enough to explain the differences in the results. To verify our results, the decay of ^{153}Tb was followed to be sure that no other radionuclides contributed to this peak counts, and the decay time was measured and resulted to be compatible with the reference data, with a mean value of $T_{1/2}^{exp} = 2.3 \pm 0.2$ d. Note that the uncertainty on this result refers to the maximum dispersion of the experimental data and it is not the error of the average, which instead stands at 6% of $T_{1/2}^{exp}$. The TALYS 1.96 simulation reproduces quite well the literature data at least up to 58 MeV. In this work, only the data relative to the Tb foils irradiated with the four highest beam energy values are presented. This is because in the other cases, the statistics of the peaks were insufficient due to the low cross-section of the reaction.

3.5. $^{154m1,m2}Tb$

^{154m1}Tb ($T_{1/2} = 9.4$ h) and ^{154m2}Tb ($T_{1/2} = 21.5$ h) are the two metastable states of ^{154g}Tb ($T_{1/2} = 22.7$ h). A simplified decay scheme is illustrated in Fig. 6: in the scheme $\alpha_{1,2}$ represents the IT branching ratios, i.e. the probabilities that metastable states decay into the ground state, that are 12.8% and 1.8% respectively.

The metastable and the ground states share most of their gamma emissions (see Table 3) that need to be separated in order to calculate each radionuclide activity. In particular, the 649.44 keV emission overlaps with the same emission from the decay ^{154m2}Tb, while the
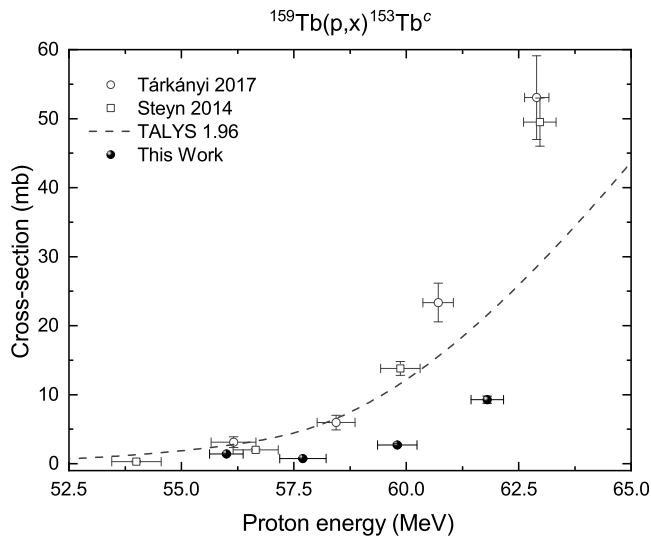
Fig. 5. Comparison between this work ^{153}Tb^c excitation function and other studies results (Tárkányi et al., 2017; Steyn et al., 2014) and the TALYS 1.96 simulation.
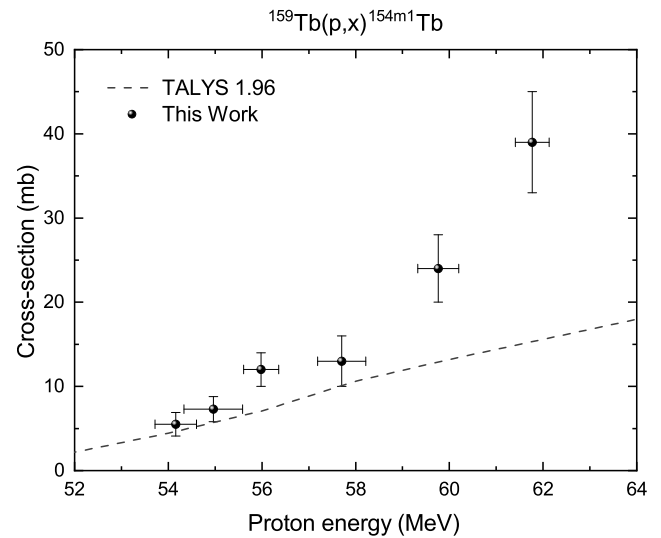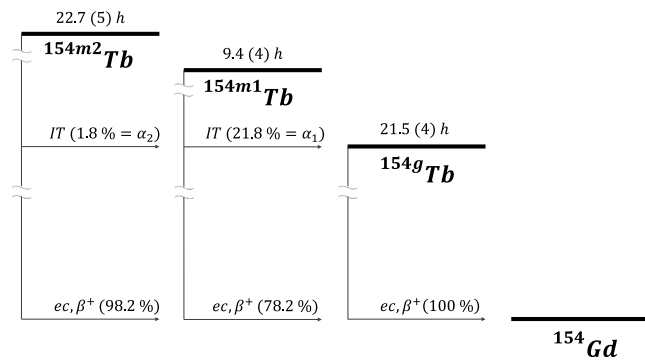

Fig. 6. Level scheme of ^{154}Tb. $\alpha_{1,2}$ are the branching ratios, i.e. the probabilities of having metastable state 1,2 decay into the ground state. Notice that the transition from the metastable state m1 to m2 is not allowed.

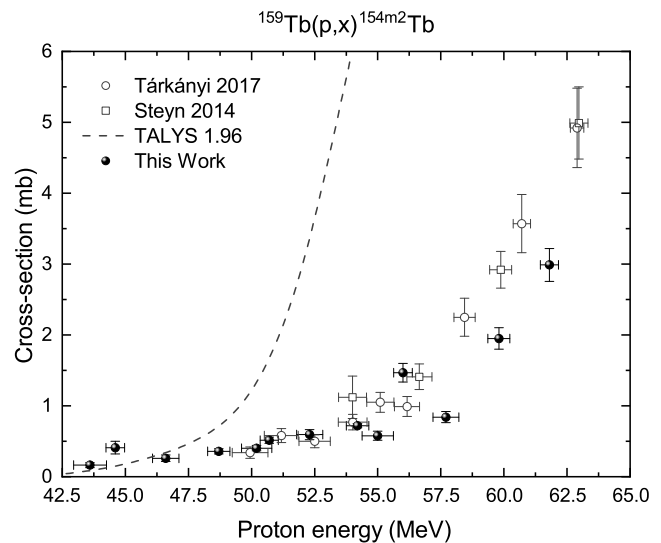**Fig. 7.** Comparison between this work ^{154m1}Tb excitation function and the TALYS 1.96 computer simulation.

Fig. 8. Comparison between this work ^{154m2}Tb excitation function and other studies results (Tárkányi et al., 2017; Steyn et al., 2014) and the TALYS 1.96 simulation.

123.07 keV and 873.21 keV emissions overlap the emissions at the same energies from both ^{154m2}Tb and ^{154g}Tb. ^{154m1}Tb has a half-life significantly different from the ^{154m2}Tb and ^{154g}Tb half-lives, meaning that the ^{154m1}Tb contribution can be separated by the ^{154m2}Tb and ^{154g}Tb contributions by performing a bi-exponential fit using Eq. (4), where $a_{1,2} = A_{m1,m2}^{EOB} \cdot I_{\gamma1,2}$. The ^{154m1}Tb and ^{154m2}Tb excitation functions shown in Figs. 7 and 8 are computed using this method.

The ^{154g}Tb direct production cross-section was determined using the following equation:

$$\sigma_g = \frac{M t_{irr} z e}{\rho x N_A Q} \frac{\lambda_g N_g^{EOB}}{H_g} + \frac{\alpha_1 \sigma_{m1}}{\lambda_g - \lambda_{m1}} \left(\lambda_{m1} - \lambda_g \frac{H_{m1}}{H_g} \right)$$
$$+ \frac{\alpha_2 \sigma_{m2}}{\lambda_g - \lambda_{m2}} \left(\lambda_{m2} - \lambda_g \frac{H_{m2}}{H_g} \right) \tag{7}$$

where $H_i(t) = (1 - e^{-\lambda_i t_{irr}})$, and

$$\lambda_g N_g^{EOB} = A_g(t) e^{\lambda_g t} + \frac{\alpha_1 A_{m1}^{EOB} e^{-\lambda_{m1} t}}{\lambda_g - \lambda_{m1}} \left(\lambda_g e^{\lambda_{m1} t} - \lambda_{m1} e^{\lambda_g t} \right)$$
$$+ \frac{\alpha_2 A_{m2}^{EOB} e^{-\lambda_{m2} t}}{\lambda_g - \lambda_{m2}} \left(\lambda_g e^{\lambda_{m2} t} - \lambda_{m2} e^{\lambda_g t} \right) \tag{8}$$

The activity $A_g(t)$ was determined using the emissions at 1291.31 keV and 1274.436 keV. The latter was used after the complete decay of ^{154m1}Tb and considering the peak of ^{22}Na (T$_{1/2}$ = 2.6018 y, E$_\gamma$ = 1274.537 keV, I$_\gamma$ = 99.940%) as a constant background, discriminated

by fitting the activity as function of time. Nonetheless, the calculated ^{154g}Tb cross-section values were compatible with zero on all targets. It must be noted that the uncertainties in the nuclear data for this radionuclide of terbium are quite high (see Table 3). Nuclear studies are therefore required to precisely assess the cross-sections of these reactions. Furthermore, the ^{154g}Tb half-life (21.5 h) is similar to the ^{154m2}Tb half-life (22.7 h), so it is not correct to talk about a cumulative ^{154g}Tb cross-section since the condition of complete decay of the parent radionuclide is not achievable.

In this work, regarding ^{154m1}Tb, only the data relative to the first two stacks are presented (Fig. 7). This is because, for lower beam energies, the gamma lines associated with this radionuclide were not visible anymore at the time of the measurement.

No previous data were present for ^{154m1}Tb production cross-sections, while in the case of ^{154m2}Tb, there is agreement with previous experiments only up to 56 MeV. The TALYS 1.96 simulation does not seem to accurately reproduce the experimental results.
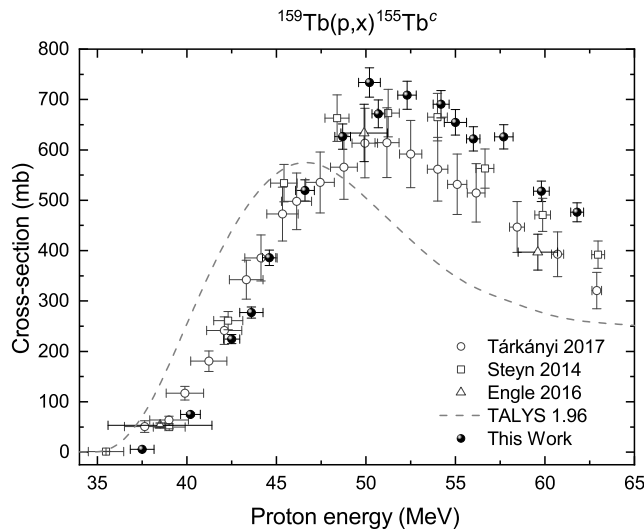
Fig. 9. Comparison between this work ^{155}Tb^c excitation function and other studies results (Tárkányi et al., 2017; Steyn et al., 2014; Engle et al., 2016) and the TALYS 1.96 simulation.
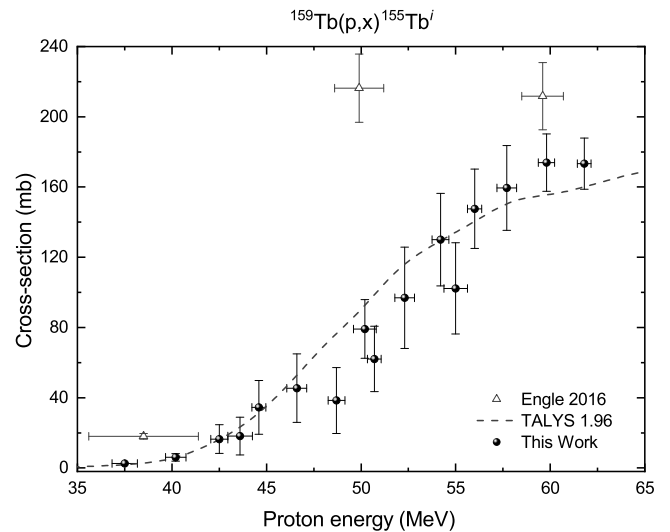

Fig. 10. Comparison between this work ^{155}Tb^i excitation function and other studies results (Engle et al., 2016) and the TALYS 1.96 simulation.

3.6. ^{155}Tb

The ^{155}Tb excitation functions, both cumulative (^{155}Tb^c) and independent (^{155}Tb^i), are shown in Figs. 9 and 10. The cumulative excitation function accounts also for the contribution of the ^{155}Dy decay into ^{155}Tb, while the independent excitation function accounts for the directly produced ^{155}Tb only (via the nuclear reaction listed in Table 3).

To separate the direct ^{155}Tb contribution and the ^{155}Dy decay contribution to the excitation function of ^{155}Tb^i the following equation for the independent cross-section was used (Colucci et al., 2023):

$$\sigma_2 = \frac{M t_{irr} z e}{\rho x N_A Q} \frac{\lambda_2 N_2^{EOB}}{H_2(t_{irr})} - \frac{\sigma_1}{\lambda_2 - \lambda_1} \left(\lambda_2 \frac{H_1(t_{irr})}{H_2(t_{irr})} - \lambda_1 \right) \quad (9)$$

where the terms with subscript 1 are referred to ^{155}Dy, while the terms with subscript 2 are referred to ^{155}Tb. In particular, $H_{1,2}(t) = (1 - e^{-\lambda_{1,2} t_{irr}})$, and $\lambda_2 N_2^{EOB}$ term was determined by solving the Bateman equations and calculated with the following formula:

$$\lambda_2 N_2^{EOB} = A_2(t_{dec}) e^{\lambda_2 t_{dec}} - \frac{A_1(t_{dec})}{\lambda_2 - \lambda_1} \left(\lambda_1 e^{\lambda_2 t_{dec}} - \lambda_2 e^{\lambda_1 t_{dec}} \right) \quad (10)$$

where t_{dec} is the time elapsed between EOB and the start of measurement. TALYS 1.96 simulation seems to agree with the excitation function of ^{155}Tb^i measured this work, low accordance is present with Eagle's data (Engle et al., 2016).

Major accordance is present between the results of this work and the data of the previous studies in the case of the cumulative cross-section, TALYS simulation seems to be shifted to lower energies. The results of the independent cross-section are in good agreement with the theoretical calculations but Engle's data (Engle et al., 2016) overestimates our results.

3.7. ^{156g}Tb^c

Fig. 11 shows the ^{156}Tb cumulative (^{156}Tb^c) excitation function. This excitation function is presented as cumulative because it also includes the contribution of the ^{156m1}Tb ($T_{1/2} = 24.4$ h) and ^{156m2}Tb metastable states ($T_{1/2} = 5.3$ h), which decay into ^{156g}Tb. It was not possible to measure the activity of ^{156m1}Tb, and thus separate the different contributions to the cumulative cross-section, due to a superposition between its only gamma emission ($E_\gamma = 49.630$ *10* keV, $I_\gamma\% = 74.1$ *3*) and the characteristic X-rays emissions of all the produced

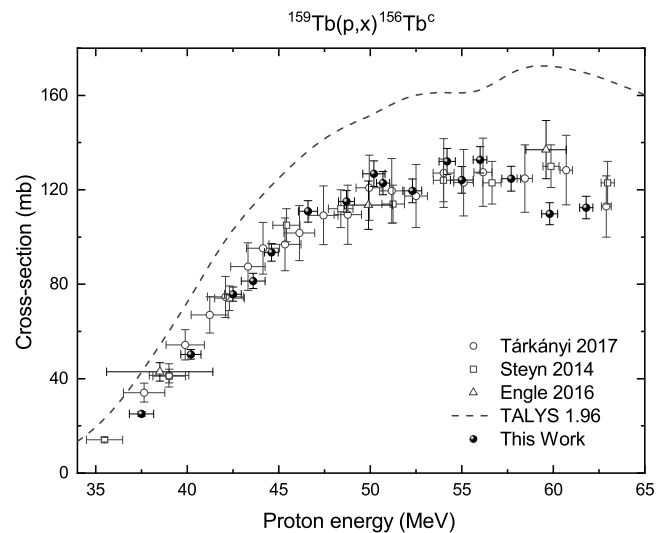**Fig. 11.** Comparison between this work ^{156}Tb^c excitation function and other studies results (Tárkányi et al., 2017; Steyn et al., 2014; Engle et al., 2016) and the TALYS 1.96 simulation.

Tb radioisotopes (with energies ranging between approximately 42 and 50 keV), moreover, it was not possible to calibrate the detector at such a low energy. In the case of ^{156m2}Tb, the measure was not possible due to the short decay time and to the fact that it only presents a single gamma emission with unknown intensity ($E_\gamma = 88.4$ *10* keV, $I_\gamma\% < 1.15$). The measurements for the determination of the ^{156g}Tb cumulative excitation function were carried out only 9 days after EOB, in order to wait for at least 7–8 ^{156m1}Tb half-lives to be close to the condition of full decay of the metastable state.

The TALYS 1.96 simulation does not seem to accurately reproduce the experimental data for energies above 40–45 MeV, while the accordance with the other works is good.

3.8. ^{151}Gd^c

The ^{151}Gd cumulative excitation function is presented in Fig. 12, where it can be seen that our work data match well the data of Steyn and its collaborators (Steyn et al., 2014). The TALYS 1.96 simulation, on the other hand, does not seem to agree with experimental data.
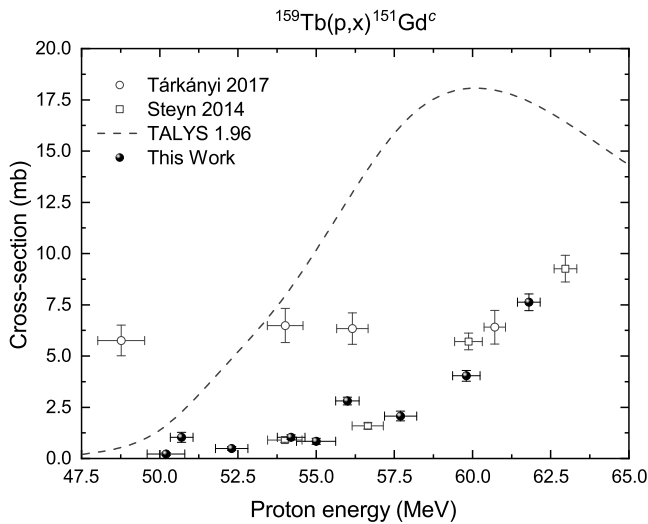
Fig. 12. Comparison between this work ^{151}Gd^c excitation function and other studies results (Tárkányi et al., 2017; Steyn et al., 2014) and the TALYS 1.96 simulation.
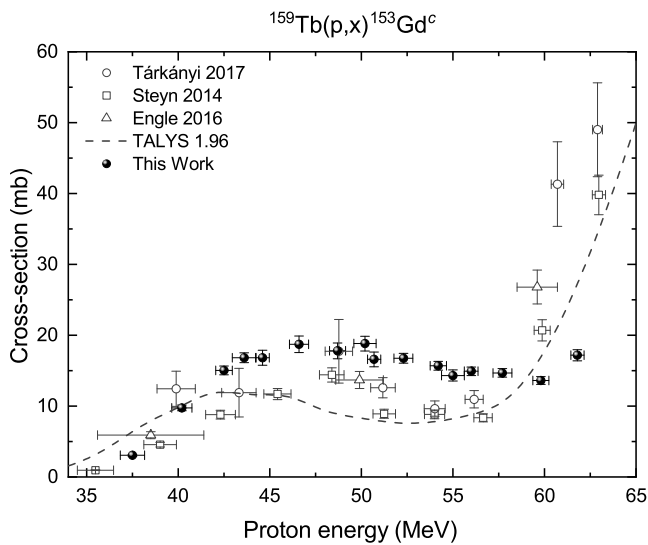

Fig. 13. Comparison between this work ^{153}Gd^c excitation function and other studies results (Tárkányi et al., 2017; Steyn et al., 2014; Engle et al., 2016) and the TALYS 1.96 simulation.

3.9. ^{153}Gd

The ^{153}Gd cumulative (^{153}Gd^c) excitation function is reported in Fig. 13. It also includes the contribution of the parent radionuclides decay (i.e. ^{153}Tb and ^{153}Dy). The results of this work follows the same trend of the other studies in literature (Tárkányi et al., 2017; Steyn et al., 2014; Engle et al., 2016) and of the TALYS 1.96 simulation for energies below 55 MeV, however the whole dataset results scattered.

4. Yield of the indirectly produced ^{155}Tb

As described by Moiseeva et al. (2022), one of the possibilities to produce pure ^{155}Tb is from the decay of ^{155}Dy. This production route is referred to as indirect production or precursor: the dysprosium is produced with some nuclear reactions, in this case ^{159}Tb(p,5n); the target is dissolved and a first radiochemical separation permits to isolate of the Dy isotopes (^{155}Dy and its isotopic contaminants); then, after a certain time during which ^{155}Dy decays in ^{155}Tb, a second

radiochemical separation must be performed to extract the decay-produced terbium isotopes (^{155}Tb and its isotopic contaminants) from dysprosium (in particular the long-lived ^{159}Dy and ^{154}Dy).

The End of Bombardment Thick Target Yield ($TTY(E; \Delta E; t_{irr})$ (MBq µA^{-1})) (Otuka and Takács, 2015) of the Dy radionuclides was determined using the following formula (Pupillo et al., 2022):

$$TTY_{Dy}^{EOB}(E; \Delta E; t_{irr}) = \frac{N_A \cdot (1 - e^{-\lambda t_{irr}})}{M \cdot \mathbf{e}} \int_{E-\Delta E}^{E} \frac{\sigma(E')}{\frac{1}{\rho}\frac{dE}{dx}(E')} dE' \quad (11)$$

where E is the incident proton beam energy, ΔE is the energy loss in the thick target, $\frac{1}{\rho}\frac{dE}{dx}$ is the mass stopping power of protons in the thick target material, while N_A, M and $\mathbf{e}$ were defined in Eq. (1). In practice, different ΔE corresponds to different Tb target thicknesses.

In order to evaluate the feasibility of the ^{155}Dy/^{155}Tb indirect production system and to optimize the production yield from a theoretical point of view, a few assumptions have been made:

- the first separation of the produced Dy isotopes from all the radionuclides produced on the irradiated targets is hypothesized to be at $t_{sep} = 1$ h from EOB, a reasonable time to move and dissolve the target
- the daughter radionuclide is recovered when its activity is maximum. For ^{155}Tb this happens around $t_m = 40$ h after the Dy separation (Steyn et al., 2014)
- Both radiochemical separations have been considered ideal, with a 100% chemical yield.

With these assumptions, the activity per unit of beam current of ^{155}Tb indirectly produced at the End Of Separation (a_{Tb}^{EOS} (MBq µA^{-1})), i.e. of ^{155}Tb produced from ^{155}Dy decay and ^{157}Tb produced from ^{157}Dy decay, can be estimated by using the equation of the radioactive decay:

$$a_{Tb}^{EOS} = \frac{\lambda_{Tb}(e^{-\lambda_{Tb}t_m} - e^{-\lambda_{Dy}t_m})}{\lambda_{Dy} - \lambda_{Tb}} \cdot TTY_{Dy}^{EOB} \cdot e^{-\lambda_{Dy}t_{sep}} \quad (12)$$

The a_{155Tb}^{EOS} is reported in Fig. 14, where an irradiation time of 30 h has been selected. This time corresponds to about 3 half-life of ^{155}Dy and allows to obtain 90% of the maximum yield according to Eq. (11), longer irradiation time would not be advantageous being close to the saturation limit. The maximum of the activity is produced on the edge of the investigated energy range, i.e. $(E; \Delta E) = (62 \text{ MeV}; 24 \text{ MeV})$, where a yield of about 1.6 GBq µA^{-1} can be obtained.

When generating ^{155}Dy through the ^{159}Tb(p,5n) reaction, co-produced dysprosium radioisotopes (^{153,154,157,159}Dy) are formed. ^{154}Dy undergoes alpha decay with an extended half-life ($T_{1/2} = 3.0 \cdot 10^6$ y), and it does not give rise to terbium isotopes. This characteristic is significant in preserving the radionuclidic purity (RNP) and Specific Activity of the final product.

The decay of ^{157}Dy ($T_{1/2} = 8.14$ h) produces ^{157}Tb ($T_{1/2} = 71$ y), and due to its prolonged half-life, it has minimal impact on the RNP. ^{159}Dy ($T_{1/2} = 144.4$ d) only partially decays within the initial 40 h post-irradiation, limiting its contribution to Specific Activity reduction. Additionally, it produces the stable terbium isotope, ^{159}Tb, which does not affect the RNP. Nonetheless, it must be noted that the presence of ^{159}Tb in the final product in a real process, where the hypothesis of ideal radiochemical separation does not apply, will be mainly due to incomplete elimination of Tb target nuclei from the produced Dy.

However, ^{153}Dy ($T_{1/2} = 6.4$ h) may impose constraints on the maximum achievable RNP and Specific Activity above 50 MeV ($E_{th}(^{159}$Tb$(p, 7n)^{153}$Dy) = 49.9 MeV). Indeed, it decays with a half-life similar to the one of ^{155}Dy, producing a terbium radioisotope, ^{153}Tb ($T_{1/2} = 2.34$ d), whose decay time is comparable to the one of ^{155}Tb.

Unfortunately, due to the delayed start of measurements (2 days post-irradiation), the cross-section of ^{153}Dy production remains unmeasured. Consequently, a comprehensive theoretical characterization in terms of RNP and Specific Activity of this indirect system is currently unattainable.

Table 6

Comparison between the TTY of ^{155}Tb obtainable using different nuclear reactions (Dellepiane et al., 2022; Wang et al., 2023). The physical yield is not defined for the indirect production process. The TTY is reported for an irradiation of 30 h for all the reactions presented.

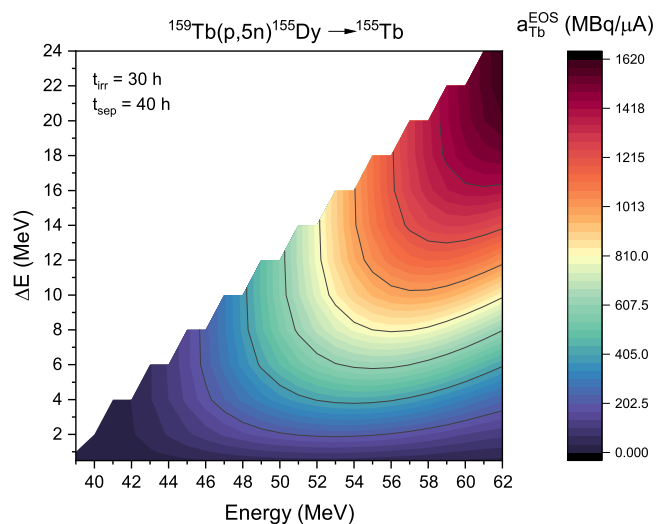| Process	E_{in} (MeV)	Target form	Target thickness (μm)	α_{phys} (MBq μA^{-1} h^{-1})	TTY (30 h) (MBq μA^{-1})	Max RNP (%)
^{155}Gd(p,n) (Dellepiane et al., 2022)	10.5	(^{155}Gd)Gd$_2$O$_3$	300	3.4 ± 0.2	95	93
^{156}Gd(p,2n) (Dellepiane et al., 2022)	18.5	(^{156}Gd)Gd$_2$O$_3$	300	14.3 ± 0.7	400	89
^{155}Gd(d,2n) (Wang et al., 2023)	15.1	(^{155}Gd)Gd$_2$O$_3$	390	10.2 ± 0.7	280	89
^{159}Tb(d,5n) ^{155}Dy→^{155}Tb	62	metallic Tb	4500	–	1600	–

Fig. 14. Activity per unit of current of ^{155}Tb at the EOS from ^{155}Dy, as a function of the incident proton beam energy and of the loss of energy within the target. A 30-h long irradiation has been assumed. The time between the two radiochemical separations has been set to 40 h to maximize the amount of terbium activity.

A comparison between the yield of direct production of ^{155}Tb via ^{155}Gd(p,n), ^{156}Gd(p,2n) (Dellepiane et al., 2022), ^{155}Gd(d,2n) (Wang et al., 2023) direct processes and the production yield of the indirect process is reported in Table 6. The indirect production yield is sensibly higher even though thicker targets and higher energy protons are required. Nonetheless, expensive enriched targets are not required since terbium is naturally monoisotopic. The results in previous works have been presented in terms of physical yield, α_{phys} (MBq μA^{-1} h^{-1}), that can be transformed in TTY for a given irradiation time by using the relation (Otuka and Takács, 2015):

$$TTY(t_{irr}) = \frac{\alpha_{phys}}{\lambda} \cdot \left(1 - e^{-\lambda t_{irr}}\right) \qquad (13)$$

As previously discussed, the purity of the indirect process is to be determined and probably will require to shift the entrance energy below the energy threshold of production of ^{153}Dy ($E_{th}(^{159}$Tb$(p,7n)^{153}$Dy) = 49.9 MeV) with a reduction of the maximum yield.

5. Conclusions

The excitation functions of the radionuclides produced via the ^{159}Tb(p,x) nuclear reaction were measured in the 37.5–62 MeV beam energy interval. The obtained data were compared with other studies which carried out similar procedures (Tárkányi et al., 2017; Steyn et al., 2014; Engle et al., 2016) and with the TALYS 1.96 simulation (ran with default settings). This comparison resulted in a general agreement between this study and previous studies' data for most of the analyzed radionuclides. Particular attention was given to the directly produced Dy radionuclides in order to evaluate the feasibility of a ^{155}Dy/^{155}Tb precursor system.

The potential for ^{155}Tb production using a Dy/Tb indirect production system was explored. The yield of the eluted Tb isotopes was evaluated by hypothesizing two radiochemical separations: the first separation was necessary to separate the directly produced Dy isotopes from the irradiated targets 1 h after EOB, while the second separation was necessary to isolate the decay-produced Tb isotopes from the ^{155}Dy/^{155}Tb precursor system 40 h after the first separation (i.e. the time at which the ^{155}Tb activity is maximum). For a 30 h irradiation, the maximum ^{155}Tb yield was calculated to be 1.6 GBq μA^{-1}.

The directly produced ^{159}Dy lead to the production of ^{159}Tb, whose presence may affect the specific activity, since part of the radiopharmaceuticals will be radiolabeled with stable isotope. However, being the half-life of ^{159}Dy very long compared to the decay time of ^{155}Dy its production rate is slow according to Eq. (11), and also the number of ^{159}Tb nuclei produced is low during the decay time of 40 h, not affecting the Specific Activity significantly. At the same time the radionuclidic purity is not influenced significantly by ^{157}Tb since its half-life (71 years) is much longer compared to the ^{155}Tb half-life (5.32 days). Notably, ^{154}Dy's alpha decay, with an extended half-life ($T_{1/2} = 3.0 \cdot 10^6$ y), does not lead to terbium isotope formation, crucial for preserving radionuclidic purity and Specific Activity. However, ^{153}Dy ($T_{1/2} = 6.4$ h) could limit the maximum achievable Radionuclidic Purity (RNP) and Specific Activity ($E_{th}(^{159}$Tb$(p,7n)^{153}$Dy) = 49.9 MeV). Its decay yields to ^{153}Tb ($T_{1/2} = 2.34$ d), whose decay time is comparable to ^{155}Tb's decay time. Unfortunately, due to delayed measurements (initiated 2 days post-irradiation), the cross-section of ^{153}Dy production remains unmeasured. A comprehensive theoretical characterization of this indirect system, concerning RNP and Specific Activity, is currently unattainable. Moreover, in a real process where ideal radiochemical separation is not assumed, the presence of ^{159}Tb will primarily result from incomplete removal of Tb target nuclei from the produced Dy. This will probably represent the main component of reduction of the Specific Activity of the final product.

In conclusion, the experimental excitation function measured in this study will enrich the nuclear data on Tb radionuclides, allowing for better theoretical calculations for these nuclei. Furthermore, the study of the yield of the indirectly produced ^{155}Tb gives promising estimations for implementation of the ^{155}Dy/^{155}Tb precursor system. Studies about the shape, composition, and stability of the targets, the achievable RNP and the Specific Activity, and the radiochemical separation of terbium and dysprosium on a large scale are still required for a better understanding of the feasibility of the aforementioned precursor system.

CRediT authorship contribution statement

Michele Colucci: Writing – review & editing, Writing – original draft, Methodology, Investigation, Formal analysis, Data curation, Conceptualization. **Filippo Carlo Bolchini:** Writing – original draft, Investigation, Formal analysis, Data curation. **Lorenzo Confalonieri:** Writing – review & editing, Visualization, Formal analysis. **Ferid Haddad:** Writing – review & editing, Resources, Funding acquisition. **Etienne Nigron:** Writing – review & editing, Investigation. **Flavia Groppi:** Writing – review & editing, Validation, Supervision, Resources, Project administration, Funding acquisition, Conceptualization. **Simone Manenti:** Writing – review & editing, Validation, Supervision, Project administration, Conceptualization.

Declaration of competing interest

The authors declare that they have no known competing financial interests or personal relationships that could have appeared to influence the work reported in this paper.

Data availability

Data will be made available on request.

Acknowledgments

References

Colucci, M., Carminati, S., Haddad, F., Nigron, E., Groppi, F., Manenti, S., 2022. Excitation functions of deuteron induced nuclear reactions on dysprosium targets for the production of the theranostic relevant isotopes of terbium. Eur. Phys. J. Plus 137 (10), http://dx.doi.org/10.1140/epjp/s13360-022-03378-z.

Colucci, M., Groppi, F., Manenti, S., 2023. Decoupling of radionuclide production cumulative cross-sections and TTY: Application to the process $^{nat}Dy(d, x)^{155}Ho \rightarrow {}^{155}Dy \rightarrow {}^{155}Tb$. Il Nuovo Cimento Soc. Ital. Fis. C Colloq. Commun. Phys. 46 (4), http://dx.doi.org/10.1393/ncc/i2023-23129-3.

Dellepiane, G., Casolaro, P., Favaretto, C., Grundler, P.V., Mateu, I., Scampoli, P., Talip, Z., van der Meulen, N.P., Braccini, S., 2022. Cross section measurement of terbium radioisotopes for an optimized ^{155}Tb production with an 18 MeV medical PET cyclotron. Appl. Radiat. Isot. 184, 110175. http://dx.doi.org/10.1016/j.apradiso.2022.110175.

Engle, J.W., Mashnik, S.G., Parker, L.A., Jackman, K.R., Bitteker, L.J., Ullmann, J.L., Gulley, M.S., Pillai, C., John, K.D., Birnbaum, E.R., Nortier, F.M., 2016. Nuclear excitation functions from 40 to 200 MeV proton irradiation of terbium. Nucl. Instrum. Methods Phys. Res. B 366 (C), 206–216. http://dx.doi.org/10.1016/j.nimb.2015.10.049.

Haddad, F., Ferrer, L., Guertin, A., Carlier, T., Michel, N., Barbet, J., Chatal, J.-F., 2008. ARRONAX, a high-energy and high-intensity cyclotron for nuclear medicine. Eur. J. Nucl. Med. Mol. Imaging 35 (7), 1377–1387. http://dx.doi.org/10.1007/s00259-008-0802-5.

Hermanne, A., Ignatyuk, A., Capote, R., Carlson, B., Engle, J., Kellett, M., Kibédi, T., Kim, G., Kondev, F., Hussain, M., Lebeda, O., Luca, A., Nagai, Y., Naik, H., Nichols, A., Nortier, F., Suryanarayana, S., Takács, S., Tárkányi, F., Verpelli, M., 2018. Reference cross sections for charged-particle monitor reactions. Nucl. Data Sheets (no. C), 338–382. http://dx.doi.org/10.1016/j.nds.2018.02.009.

Herzog, H., Rösch, F., Stöcklin, G., Lueders, C., Qaim, S.M., Feinendegen, L.E., 1993. Measurement of pharmacokinetics of yttrium-86 radiopharmaceuticals with PET and radiation dose calculation of Analogous Yttrium-90 Radiotherapeutics. J. Nucl. Med. 34 (12), 2222–2226, URL https://jnm.snmjournals.org/content/34/12/2222.

Koning, A., Rochman, D., 2012. Modern nuclear data evaluation with the TALYS code system. Nucl. Data Sheets 113 (12), 2841–2934. http://dx.doi.org/10.1016/j.nds.2012.11.002.

Koning, A., Rochman, D., Sublet, J.-C., Dzysiuk, N., Fleming, M., van der Marck, S., 2019. TENDL: Complete nuclear data library for innovative nuclear science and technology. Nucl. Data Sheets 155, 1–55. http://dx.doi.org/10.1016/j.nds.2019.01.002, Special Issue on Nuclear Reaction Data.

Lehenberger, S., Barkhausen, C., Cohrs, S., Fischer, E., Grünberg, J., Hohn, A., Köster, U., Schibli, R., Türler, A., Zhernosekov, K., 2011. The low-energy β^- and electron emitter ^{161}Tb as an alternative to ^{177}Lu for targeted radionuclide therapy. Nucl. Med. Biol. 38 (6), 917–924. http://dx.doi.org/10.1016/j.nucmedbio.2011.02.007.

Moiseeva, A., Aliev, R., Furkina, E., Novikov, V., Unezhev, V., 2022. New method for production of ^{155}Tb via ^{155}Dy by irradiation of ^{nat}Gd by medium energy alpha particles. Nucl. Med. Biol. 106–107, 52–61. http://dx.doi.org/10.1016/j.nucmedbio.2021.12.004.

Moiseeva, A., Makoveeva, K., Furkina, E., Artyushova, E., German, M., Khomenko, I., Konevega, A., Kormazeva, E., Novikov, V., Aksenov, N., Gustova, N., Aliev, R., 2023. Co-production of ^{155}Tb and ^{152}Tb irradiating ^{155}Gd / ^{151}Eu tandem target with a medium energy α-particle beam. Nucl. Med. Biol. 126–127, 108389. http://dx.doi.org/10.1016/j.nucmedbio.2023.108389.

Müller, C., Domnanich, K.A., Umbricht, C.A., van der Meulen, N.P., 2018. Scandium and terbium radionuclides for radiotheranostics: current state of development towards clinical application. Br. J. Radiol. 91 (1091), 20180074. http://dx.doi.org/10.1259/bjr.20180074.

Müller, C., Umbricht, C.A., Gracheva, N., Tschan, V.J., Pellegrini, G., Bernhardt, P., Zeevaart, J.R., Köster, U., Schibli, R., van der Meulen, N.P., 2019. Terbium-161 for PSMA-targeted radionuclide therapy of prostate cancer. Eur. J. Nucl. Med. Mol. Imaging 46 (9), 1919–1930. http://dx.doi.org/10.1007/s00259-019-04345-0.

Müller, C., Vermeulen, C., Köster, U., Johnston, K., Türler, A., Schibli, R., van der Meulen, N.P., 2017. Alpha-PET with terbium-149: evidence and perspectives for radiotheragnostics. EJNMMI Radiopharm. Chem. 1 (1), 5. http://dx.doi.org/10.1186/s41181-016-0008-2.

Müller, C., Zhernosekov, K., Köster, U., Johnston, K., Dorrer, H., Hohn, A., van der Walt, N.T., Türler, A., Schibli, R., 2012. A unique matched quadruplet of terbium radioisotopes for PET and spect and for α- and β–radionuclide therapy: An in vivo proof-of-concept study with a new receptor-targeted folate derivative. J. Nucl. Med. 53 (12), 1951–1959. http://dx.doi.org/10.2967/jnumed.112.107540.

Naskar, N., Lahiri, S., 2021. Theranostic terbium radioisotopes: Challenges in production for clinical application. Front. Med. 8, 675014. http://dx.doi.org/10.3389/fmed.2021.675014.

National Nuclear Data Center, ENSDF database as of January 1, 2024, Version available at https://www.nndc.bnl.gov/ensdfarchivals/.

Nedrow, J.R., Anderson, C.J., 2011. Emerging radiometals for PET imaging. In: Encyclopedia of Inorganic and Bioinorganic Chemistry. John Wiley & Sons, Ltd, Chichester, UK, pp. 1–11. http://dx.doi.org/10.1002/9781119951438.eibc2447.

Otuka, N., Takács, S., 2015. Definitions of radioisotope thick target yields. Radiochim. Acta 103 (1), 1–6. http://dx.doi.org/10.1515/ract-2013-2234.

Pupillo, G., Anselmi-Tamburini, U., Barbaro, F., Bello, M., Bortolussi, S., Boschi, A., Campostrini, M., Canton, L., Carante, M.P., Cazzola, E., Cisternino, S., Colombi, A., Colucci, M., Dominicis, L.D., Nardo, L.D., Duatti, A., Fontana, A., Gorgoni, G., Groppi, F., Haddad, F., Manenti, S., Martini, P., Meléndez-Alafort, L., Mou, L., Nigron, E., Rigato, V., Sciacca, G., Esposito, J., 2023. Research on emerging medical radionuclides from the X-sections (REMIX): The accelerator-based production of ^{47}Sc, ^{149}Tb, ^{152}Tb, ^{155}Tb and ^{161}Tb. J. Phys. Conf. Ser. 2586 (1), 012118. http://dx.doi.org/10.1088/1742-6596/2586/1/012118.

Pupillo, G., Mou, L., Manenti, S., Groppi, F., Esposito, J., Haddad, F., 2022. Nuclear data for light charged particle induced production of emerging medical radionuclides. Radiochim. Acta 110 (6–9), 689–706. http://dx.doi.org/10.1515/ract-2022-0011.

Qaim, S.M., 2019. Theranostic radionuclides: recent advances in production methodologies. J. Radioanal. Nucl. Chem. 322 (3), 1257–1266. http://dx.doi.org/10.1007/s10967-019-06797-y.

Qaim, S.M., Hussain, M., Spahn, I., Neumaier, B., 2021. Continuing nuclear data research for production of accelerator-based novel radionuclides for medical use: A mini-review. Front. Phys. 9, http://dx.doi.org/10.3389/fphy.2021.639290.

Qaim, S.M., Scholten, B., Neumaier, B., 2018. New developments in the production of theranostic pairs of radionuclides. J. Radioanal. Nucl. Chem. 318, 1493–1509. http://dx.doi.org/10.1007/s10967-018-6238-x.

Rösch, F., Herzog, H., Qaim, S.M., 2017. The beginning and development of the theranostic approach in nuclear medicine, as exemplified by the radionuclide pair ^{86}Y and ^{90}Y. Pharmaceuticals (Basel) 10 (2), 56. http://dx.doi.org/10.3390/ph10020056, PMCID: PMC5490413.

Steyn, G., Vermeulen, C., Szelecsényi, F., Kovács, Z., Hohn, A., van der Meulen, N., Schibli, R., van der Walt, T., 2014. Cross sections of proton-induced reactions on ^{152}Gd, ^{155}Gd and ^{159}Tb with emphasis on the production of selected tb radionuclides. Nucl. Instrum. Methods Phys. Res. B 319, 128–140. http://dx.doi.org/10.1016/j.nimb.2013.11.013.

Tárkányi, F., Hermanne, A., Ditrói, F., Takács, S., Ignatyuk, A., 2017. Activation cross-sections of longer lived radioisotopes of proton induced nuclear reactions on terbium up to 65 MeV. Appl. Radiat. Isot. 127, 7–15. http://dx.doi.org/10.1016/j.apradiso.2017.04.030.

Wang, Y., Sounalet, T., Guertin, A., Nigron, E., Michel, N., Haddad, F., 2023. Study of terbium production from enriched Gd targets via the reaction ^{155}Gd(d,2n)^{155}Tb. Appl. Radiat. Isot. 201, 110996. http://dx.doi.org/10.1016/j.apradiso.2023.110996.